Angewandte Chemie International Edition

Angewandte International Edition Chemie

GDCh German Chemical Society

How to cite: *Angew. Chem. Int. Ed.* **2026**, 65, e8338805
doi.org/10.1002/anie.8338805

RESEARCH ARTICLE

Creating Anionic Microenvironment Around Single-Atom Fe Sites in Metal–Organic Frameworks for Enhanced Nitrate Electroreduction

Song Chen[1] | Yunyang Qian[2] | Ziyong Cheng[1] | Lai-Hon Chung[1] | Weihui Ou[1] | Jieying Hu[1] | Quanxi Mo[1] | Shaoru Chen[1] | Jun He[1] | Hai-Long Jiang[2]

[1]School of Chemical Engineering and Light Industry, Guangdong University of Technology, Guangzhou, Guangdong, P. R. China | [2]Hefei National Research Center for Physical Sciences At the Microscale, Department of Chemistry, University of Science and Technology of China, Hefei, Anhui, P. R. China

Correspondence: Jun He (junhe@gdut.edu.cn) | Hai-Long Jiang (jianglab@ustc.edu.cn)

Received: 9 March 2026 | **Revised:** 9 March 2026 | **Accepted:** 20 March 2026

Keywords: $K^+ \cdot H_2O$ | metal–organic framework | microenvironment modulation | nitrate electroreduction | single atom

ABSTRACT

The electrocatalytic nitrate reduction reaction (eNO_3RR) offers a sustainable strategy for both NO_3^- wastewater remediation and value-added NH_3 production. However, its application is hindered by sluggish reaction kinetics in neutral media due to the limited availability of protons. Herein, an anionic metal–organic framework (MOF), SU-102, is functionalized with atomically dispersed Fe sites to yield SU-102-Fe. This catalyst achieves a Faradaic efficiency (FE) of 96.9% and NH_3 production rate of 1.72 mg h^{-1} mg_{cat}^{-1} at −0.7 V versus RHE, far surpassing the commercial Fe_2O_3 and pristine SU-102. In situ characterizations reveal that the negatively charged Zr—O units in SU-102 create an anionic microenvironment around the Fe sites, which enriches $K^+ \cdot H_2O$ species derived from the interfacial hydrogen-bonding network. The facile dissociation of $K^+ \cdot H_2O$ improves local proton supply, facilitating NO_3^--to-NH_3 conversion and accounting for the superior eNO_3RR performance of SU-102-Fe.

1 | Introduction

The global nitrogen cycle underpins ecological stability [1, 2], yet excessive NO_3^- accumulation in industrial and agricultural effluents threatens both environment and human health. Traditional nitrate removal methods, including biological denitrification and physicochemical treatments [3–6], are energy-intensive and offer limited potential for recovering valuable products [7, 8]. Electrocatalytic nitrate reduction (eNO_3RR) offers a promising alternative by converting nitrate into ammonia, thereby reducing pollution while producing useful chemicals [9–12]. With a theoretical energy consumption of only 6.5 kWh·kg^{-1} for NH_3, eNO_3RR is considerably more energy-efficient than the Haber–Bosch process (10–13 kWh·kg^{-1}) [13, 14]. Despite this advantage, existing eNO_3RR catalysts often operate at high potentials and suffer from low selectivity, generating undesired byproducts such as H_2 and nitrite (NO_2^-), which present challenges for the effective operation of eNO_3RR [15–17].

Iron (Fe)-based catalysts are widely used in eNO_3RR due to their intrinsically low activity for the hydrogen evolution reaction (HER) [18, 19]. However, the complete reduction of NO_3^- to NH_3 involves an eight-electron, nine-proton process ($NO_3^- + 8e^- + 9H^+ \rightarrow NH_3 + 3H_2O$), and insufficient proton supply can limit catalytic performance [17, 20–22]. In a neutral aqueous electrolyte, most H_2O molecules participate in hydrogen-bonded networks that prevent their dissociation into protons, thereby suppressing the hydrogenation of surface-bound NO_3RR intermediates

Song Chen and Yunyang Qian contributed equally to this work.

[23–25]. In contrast, weakly coordinated species such as potassium ion hydrated water ($K^+ \bullet H_2O$), can dissociate more readily under an applied potential and serve as more effective proton donors [26, 27]. Therefore, local enrichment and adsorption of $K^+ \bullet H_2O$ around the Fe sites may improve proton supply and facilitate reaction kinetics. Furthermore, designing Fe-based catalysts with atomically dispersed sites and high surface accessibility is essential for improving the utilization of active sites and mass transport of substrates, both of which are critical for achieving efficient nitrate reduction [28–31].

To this end, metal–organic frameworks (MOFs), a class of crystalline porous materials with tunable and well-defined structures [32–40], provide an ideal platform for stabilizing atomically dispersed metal sites [41–43]. Amongst them, anionic MOFs are particularly attractive because their negatively charged skeletons not only stabilize single-atom metal sites but also create distinctive microenvironment that facilitates the adsorption of positively charged species around metal sites [44–47]. Therefore, anchoring single-atom Fe sites onto anionic MOF skeleton would hold great promise for improving the catalytic performance of eNO_3RR, yet this strategy has not been reported. Herein, a stable anionic MOF, SU-102, has been synthesized using ellagic acid as the organic linker and Zr-oxo unit as the metal node. Through a simple post-synthetic modification, single-atom Fe sites are anchored onto the skeleton, yielding SU-102-Fe as an efficient catalyst for nitrate reduction (Scheme 1). The crystalline and porous structure of the MOF ensures spatial dispersion of Fe sites, thereby guaranteeing substrate accessibility. Additionally, the negatively charged Zr-oxo units create an anionic microenvironment that electrostatically attracts $K^+ \bullet H_2O$ species, promoting their dissociation into H^+ and improving active hydrogen (*H) supply for NO_3^- reduction. Consequently, SU-102-Fe achieves a maximum Faradaic efficiency of 96.9% and an NH_3 production rate of 1.72 mg h^{-1} mg_{cat}^{-1} at −0.7 V versus RHE. The rate is twice that of commercial Fe_2O_3 and nearly 70 times higher than that of pristine SU-102. These results demonstrate that the anionic microenvironment surrounding the Fe sites enhances eNO_3RR performance, providing a promising strategy for the design of high-efficiency nitrate electroreduction catalysts.

2 | Results and Discussion

The SU-102 ($(C_2H_8N)_2[Zr(C_{14}H_3O_8)_2] \bullet 6H_2O$) was synthesized by refluxing ellagic acid and $ZrOCl_2 \bullet 8H_2O$ (linker:metal mole ratio approximately 2:1) in a mixed solvent of *N*,*N*-dimethylformamide, CH_3COOH and ultrapure H_2O at 90°C for three days [48]. SU-102 features one-dimensional honeycomb channels, where Zr^{4+} centers exist as isolated ZrO_8 units with square antiprismatic coordination. Each Zr^{4+} is coordinated to four partially deprotonated ellagic acid anions, generating a negatively charged three-dimensional network. To maintain charge neutrality, dimethylammonium ($Me_2NH_2^+$) cations are incorporated within the pores (Figure S1). The negative charge and abundant hydroxyl groups in the Zr-oxo unit provide the potential for chelation with metal ions. Specifically, SU-102 was stirred with Fe^{3+} ions under ambient conditions, and a rapid color change from yellow to black was observed upon addition of Fe^{3+} (Figure S2). Elemental analysis confirms complete replacement of $Me_2NH_2^+$ ions with Fe^{3+} (Table S1), yielding the target catalyst SU-102-Fe (Figure S3). Notably, SU-102-Fe can be synthesized quantitatively on the gram scale, underscoring its ease of preparation and practical applicability (Figure S4).

As shown in the powder X-ray diffraction (PXRD) patterns of SU-102-Fe samples loaded with varying amounts of Fe^{3+} (Figure S5 and Table S2), the crystallinity of SU-102 is retained after Fe incorporation. The N_2 sorption isotherms of SU-102 at 77 K display a type I isotherm with a Brunauer–Emmett–Teller (BET) surface area of 545 m^2 g^{-1}, while SU-102-Fe shows a reduced BET surface area of 360 m^2 g^{-1} (Figure S6), indicating the retention of permanent porosity along with partial pore/mass occupation by Fe ions. The gram-scale SU-102-Fe maintains high crystallinity and exhibits surface area comparable to that of the small-scale material (Figures S5 and S6). The scanning electron microscope (SEM) image reveals that SU-102 exhibits a rod-shaped morphology (Figure S7). Despite a noticeable color change from yellow to black after introducing Fe^{3+} ions, SU-102-Fe retains the same morphology and particle size as SU-102. The transmission electron microscope (TEM) image of SU-102-Fe clearly displays a lattice stripe of 1.8 nm, corresponding to the (−120) crystal plane, matching that observed for SU-102 (Figures S8 and S9). Energy dispersive spectroscopy (EDS) mapping confirms the uniform distribution of Fe throughout the skeleton. The high-angle annular dark field scanning transmission electron microscope (HAADF–STEM) further reveals the absence of Fe_2O_3, FeO, or Fe nanoparticles, displaying instead discrete atomic-scale features consistent with isolated Fe and/or Zr sites (Figure 1a).

The X-ray photoelectron spectroscopy (XPS) spectrum of SU-102-Fe shows a Fe $2p_{3/2}$ binding energy at ~711.1 eV, a typical Fe^{3+} signal, confirming that no redox process occurs during the incorporation of Fe (Figure 1b). The O 1s spectra show a decrease in the intensity of the hydroxyl signal and the emergence of a new Fe–O peak at 530.3 eV upon Fe incorporation (Figure 1c), suggesting that Fe^{3+} binds to the hydroxyl groups in the skeleton [49, 50]. The Fe *K*-edge X-ray absorption near-edge structure (XANES) spectrum of SU-102-Fe further confirms the presence of Fe^{3+} in SU-102-Fe (Figure 1d), in agreement with the XPS results. The Fe *K*-edge extended X-ray absorption fine structure (EXAFS) analysis reveals a dominant peak corresponding to Fe—O coordination at 1.62 Å, with no detectable signals for Fe—Fe or Fe—O—Fe bonds (Figure 1e). EXAFS fitting indicates that Fe is six-coordinated by oxygen atoms of —O/OH_x groups from the Zr-oxo unit and H_2O molecules, forming an octahedral [FeO_6] environment (Figure 1f and Table S3). To better understand the coordination environment, wavelet transform (WT) analysis is performed on the EXAFS data for SU-102-Fe and the reference compounds (Figure 1g). The FeO and Fe_2O_3 demonstrate similar scattering patterns for Fe—O and Fe—O—Fe, whereas Fe-foil only shows the Fe—Fe signal. In contrast, the WT-EXAFS contour map of SU-102-Fe displays a single dominant signal at approximately 3.8 $Å^{-1}$, corresponding to Fe—O scattering, further supporting the formation of isolated Fe centers coordinated by ellagate ligands. Collectively, these results demonstrate that when Fe^{3+} is introduced into the negatively charged SU-102 framework, the —OH groups on SU-102 rapidly chelate with Fe^{3+}, forming SU-102-Fe with atomically dispersed Fe sites.

The eNO_3RR performance has been evaluated in a traditional three-electrode configuration with an H-type cell using a neutral

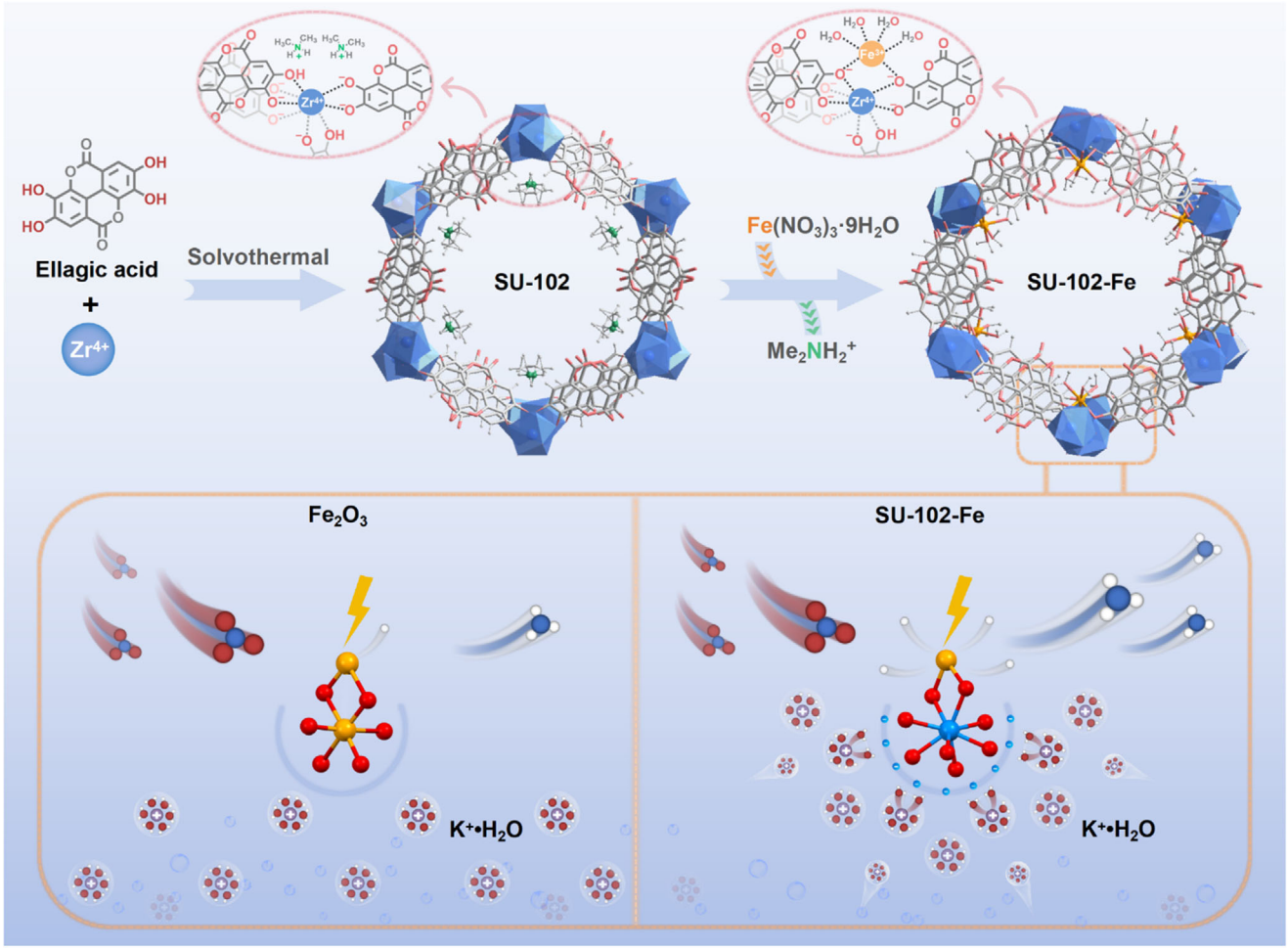

SCHEME 1 | Schematic illustration of SU-102-Fe synthesis and eNO_3RR promotion by anionic microenvironment.

electrolyte of 0.2 M K_2SO_4 and 50 mM KNO_3 under ambient conditions. The concentration of the main products of eNO_3RR is determined using UV–vis colorimetric or NMR methods with internal standards (Figures S10 and S11). The only gaseous product is hydrogen, which is determined by gas chromatography (Figure S12). Linear sweep voltammetry (LSV) curves for SU-102, SU-102-Fe, and commercial Fe_2O_3 samples reveal increased current densities in the presence of NO_3^-, confirming their eNO_3RR activity (Figure 2a). Notably, SU-102-Fe exhibits a significantly higher current density than either SU-102 or Fe_2O_3, indicating a substantial enhancement in activity upon Fe incorporation. Guided by the LSV results, chronoamperometry and colorimetric assays are conducted across a potential window of −0.5 to −1.0 V versus RHE to further evaluate catalytic performance. The FEs for NO_3^--to-NH_3 conversion display a volcano-shaped dependence on the applied potential, with SU-102-Fe outperforming both SU-102 and Fe_2O_3 at all applied voltages (Figure 2b). Specifically, SU-102-Fe achieves a maximum FE of 96.9% at −0.7 V versus RHE, which is 6.5 times higher than that of SU-102 at the same potential. In contrast, commercial Fe_2O_3 achieves a maximum NH_3 FE of 85.7% at −0.8 V versus RHE. At the same time, the NH_3 yield rate for SU-102-Fe increases with potential, reaching a yield rate of 0.86 mg h^{-1} cm^{-2} (1.72 mg h^{-1} mg_{cat}^{-1}) at −0.7 V versus RHE, representing a 60-fold enhancement over SU-102 and surpassing that of commercial Fe_2O_3 (Figure 2c). Comparable catalytic activity is also observed for the gram-scale synthesized SU-102-Fe (Figure S13). When other metal ions (Co, Ni, and Cu) are incorporated into the SU-102 framework at comparable loadings (Table S4), SU-102-Fe still delivers the highest Faradaic efficiency and NH_3 yield, highlighting the superior catalytic performance of Fe sites (Figure S14). Additionally, among MOF electrocatalysts, SU-102-Fe exhibits nearly the highest FE under neutral conditions and is superior to other reported MOF electrocatalysts (Figure 2d and Tables S5, S6). It is noteworthy that compared with SU-102, SU-102-Fe samples loaded with decreasing amounts of Fe show lower NO_2^- FE, H_2 FE and higher NH_3 FE and yield (Figures S15 and S16). These results suggest that Fe functions as the primary active site, accelerating NO_2^- reduction while inhibiting H_2 release. Furthermore, the use of Fe salts with different anions as Fe sources has little impact on catalyst preparation, as evidenced by consistent performance under identical conditions (Figure S17). These results collectively demonstrate that SU-102 serves as an effective scaffold for anchoring Fe ions, enabling the construction of efficient eNO_3RR electrocatalysts.

To evaluate the catalyst performance under varying nitrate concentrations, electrolysis experiments have been conducted using SU-102-Fe in 1–100 mM KNO_3 solutions at −0.7 V versus RHE potential. Notably, the catalyst can preserve over 80%

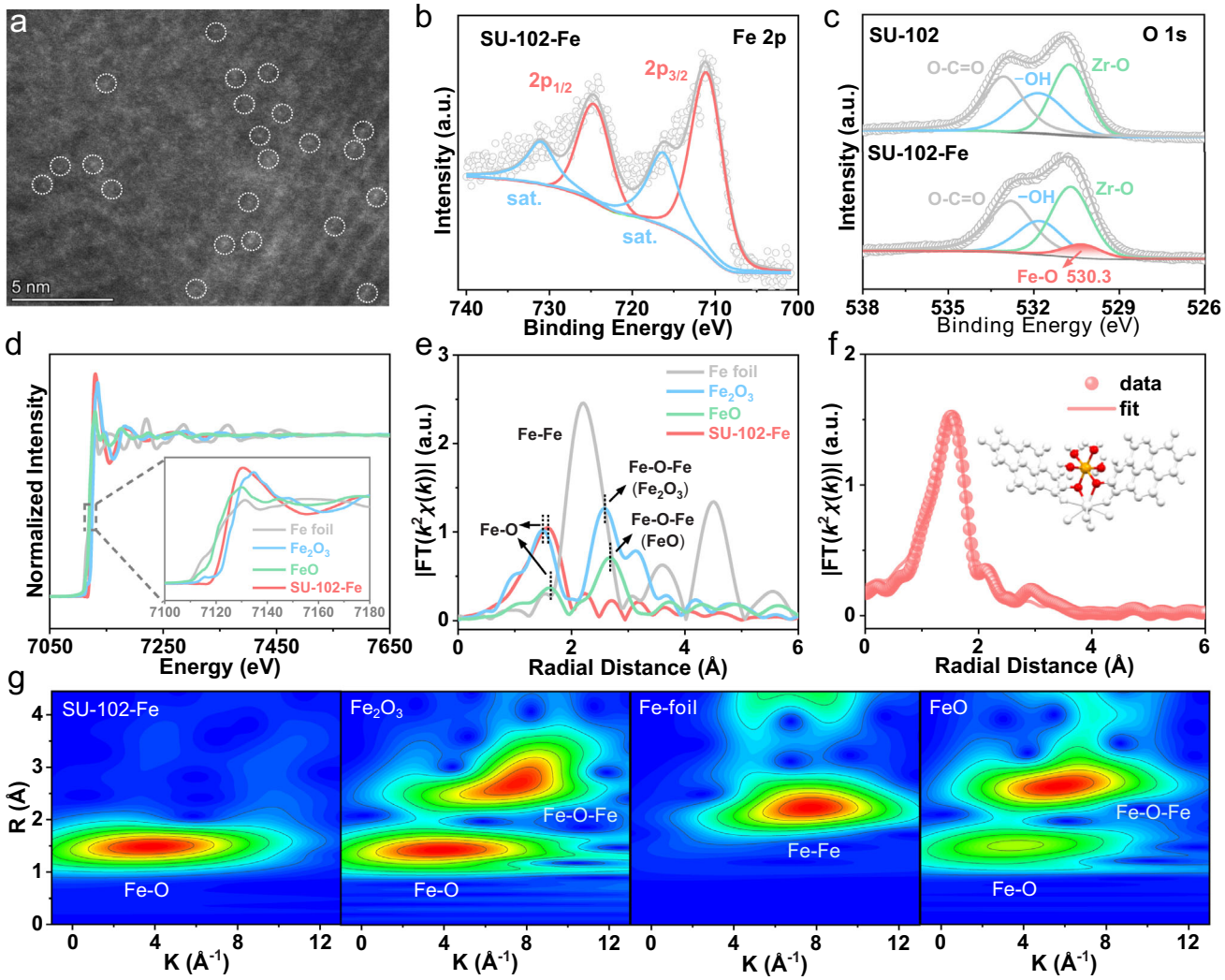

FIGURE 1 | (a) HAADF–STEM image of SU-102-Fe (single Fe/Zr atoms identified as dotted circles). (b) Fe 2p XPS spectrum of SU-102-Fe. (c) O 1s XPS spectra of SU-102 and SU-102-Fe. The Fe *K*-edge (d) XANES and (e) EXAFS spectra of SU-102-Fe, Fe_2O_3, FeO and Fe foil. (f) Fe *K*-edge EXAFS spectrum fitting of SU-102-Fe and (inset) optimized configuration for Fe (yellow: Fe, red: O, white: other atoms). (g) Wavelet transform plots for the Fe element in SU-102-Fe, Fe_2O_3, FeO and Fe foil.

NH_3 FE at a concentration as low as 10 mM, indicating its strong potential for practical applications (Figure S18). Beyond concentration effects, SU-102-Fe also maintains high selectivity in a simulated industrial wastewater containing suspended solids, chemical oxygen demand, representative co-existing anions, and heavy metal cations [51–54], delivering a Faradaic efficiency of 92.93% at −0.7 V versus RHE, with less than 3% loss compared to a pure-water-based electrolyte of identical nitrate concentration (Figures S19, S20 and Table S7). In addition to activity, long-term stability is crucial for evaluating electrocatalysts. SU-102-Fe and SU-102-Fe (gram-scale) demonstrate highly stable current density, NH_3 output, and FE over 10 h of continuous electrolysis (Figures S21 and S22). Post-electrolysis characterization further confirms the preservation of morphology and crystallinity (Figures S23 and S24), underscoring the structural robustness of the catalyst. Inductively coupled plasma (ICP) analysis shows negligible Fe leaching into the electrolyte after electrolysis in both pure nitrate solution and simulated wastewater, while the Fe content remaining on the MOF catalyst is nearly unchanged, confirming the strong immobilization of Fe species on the framework (Tables S8 and S9). XANES and EXAFS analyses of the post-reaction catalyst reveal that the Fe centers in SU-102-Fe retain their +3 oxidation state and exhibit negligible changes in coordination numbers (Figure S25 and Table S3), confirming that the Fe coordination environment remains structurally intact during catalysis. Moreover, the consistent NH_3 yields obtained over 14 alternating electrolysis cycles with and without nitrate verify the electrolyte as the nitrogen source and highlight the exceptional durability of SU-102-Fe (Figures 2e and S26).

Control experiments were conducted to verify the origin of the produced NH_3. Without applied current or in the absence of NO_3^- electrolyte, no NH_3 was detected during electrolysis, excluding the possibility of external contamination. Furthermore, carbon paper and acetylene black alone contributed negligibly to NH_3 formation (Figure S27). Isotope-labeling experiments using $^{15}NO_3^-$ or $^{14}NO_3^-$ as the nitrogen source, analyzed by ^1H NMR spectroscopy, yielded distinct doublet and triplet signals corresponding to $^{15}NH_4^+$ and $^{14}NH_4^+$, respectively (Figure 2f) [55, 56]. Time-resolved ^1H NMR spectra during prolonged electrolysis

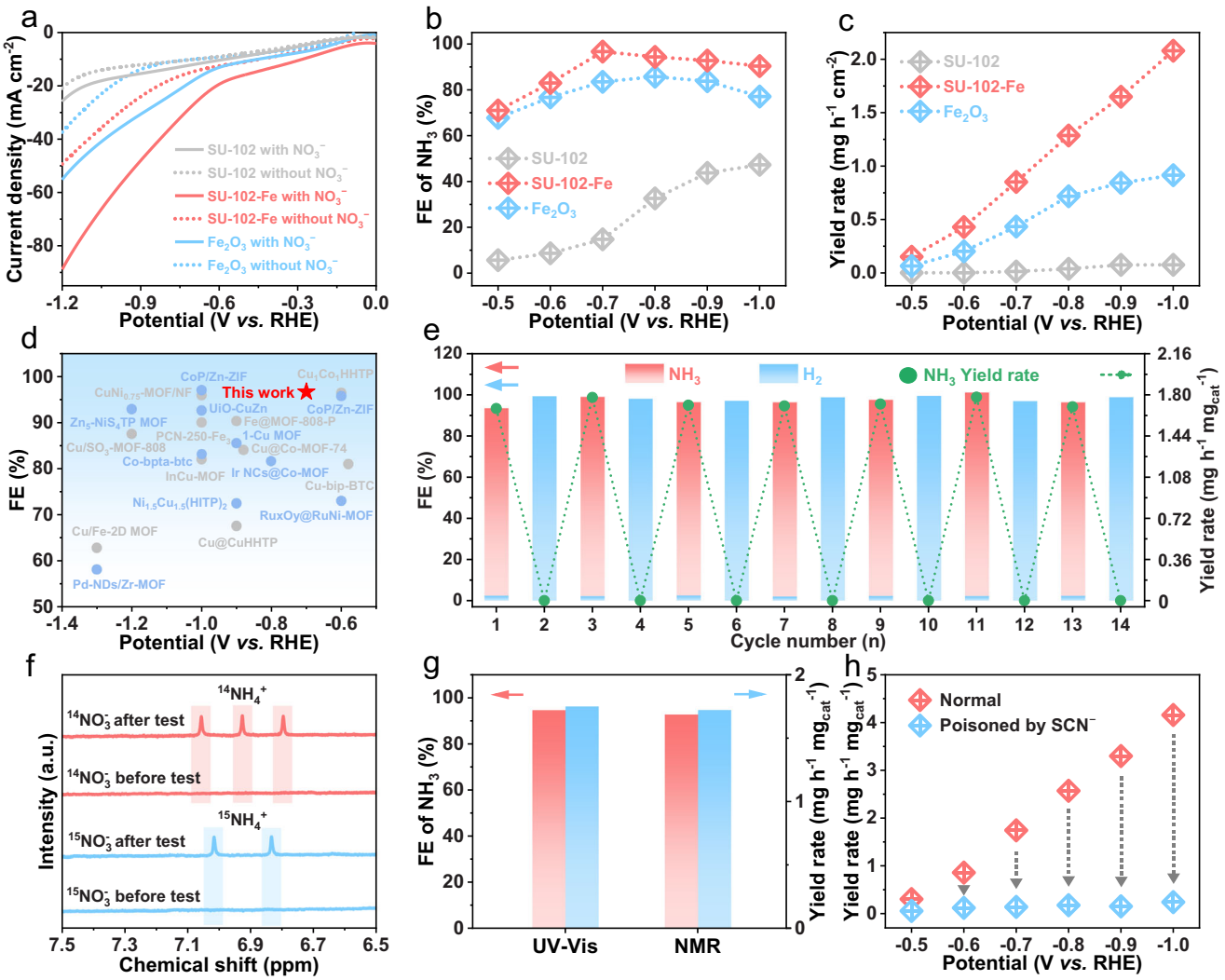

FIGURE 2 | (a) LSV curves of SU-102, SU-102-Fe and Fe_2O_3 samples in 0.2 M K_2SO_4 with/without 50 mM NO_3^-. (b) FEs and (c) NH_3 yield rates of SU-102, SU-102-Fe and Fe_2O_3 samples in eNO_3RR experiments. (d) Comparison of the eNO_3RR performance under neutral conditions by SU-102-Fe with reported MOF electrocatalysts. (e) The NH_3 FE, H_2 FE and NH_3 yield rates of SU-102-Fe over 14 alternating cycles with/without NO_3^-. (f) Isotopic labeling experiments with $^{15}NO_3^-$ and $^{14}NO_3^-$ as N sources before and after electrolysis over SU-102-Fe. (g) Quantification comparison of FEs and NH_3 yield using UV–vis chromogenic and NMR internal standard methods. (h) NH_3 yield rate for SU-102 before and after SCN^- poisoning.

confirm the continuous formation of NH_4^+ from both labeled nitrate sources (Figure S28), demonstrating sustained catalytic activity and verifying the nitrogen origin of NH_3. Further characterization shows that NH_3 is the only nitrogen-containing product after prolonged electrolysis (Figure S29), with no evidence of catalyst degradation or MOF skeleton dissolution. The excellent agreement between NMR-based quantification and colorimetric results affirms the reliability of the NH_3 detection methods (Figure 2g). To probe the active site responsible for eNO_3RR, SCN^- is introduced as a poisoning agent. A significant drop in NH_3 yield upon SCN^- treatment of SU-102-Fe indicates that Fe centers serve as the primary active sites (Figure 2h). Electrochemical impedance spectroscopy (EIS) further supports this conclusion, as SU-102-Fe exhibits the lowest charge transfer resistance among the investigated samples (Figure S30). Additionally, SU-102-Fe shows a markedly higher electrochemically active surface area (ECSA) than both SU-102 and Fe_2O_3, consistent with its superior intrinsic activity for eNO_3RR (Figure S31).

To elucidate the eNO_3RR mechanism of SU-102-Fe, attenuated total reflection Fourier transform infrared spectroscopy (ATR–FTIR) is employed to monitor surface-bound intermediates during electrolysis (Figure S32). A characteristic peak at 1365 cm^{-1}, attributed to adsorbed *NO_3 species, is clearly observed on SU-102 but nearly absent on SU-102-Fe and Fe_2O_3 (Figures 3a–c), indicating that SU-102, lacking active metal sites, accumulates *NO_3 due to slower reaction kinetics, whereas SU-102-Fe and Fe_2O_3 facilitate its efficient transformation [57, 58]. For SU-102-Fe, emerging distinct peaks of *NO_2 and *NO at ~1194 and 1264 cm^{-1} signify the involvement of these intermediates in the early stages of NH_3 formation [27, 59, 60]. Moreover, characteristic peaks at ~1064 and 1100 cm^{-1}, respectively assigned to *NH_2 and *NH_3 [61–63], appear strongly on SU-102-Fe, moderately on Fe_2O_3, and are nearly absent on SU-102, especially as electrolysis progresses. This trend underscores the superior ability of SU-102-Fe to drive the complete reduction pathway toward NH_3.

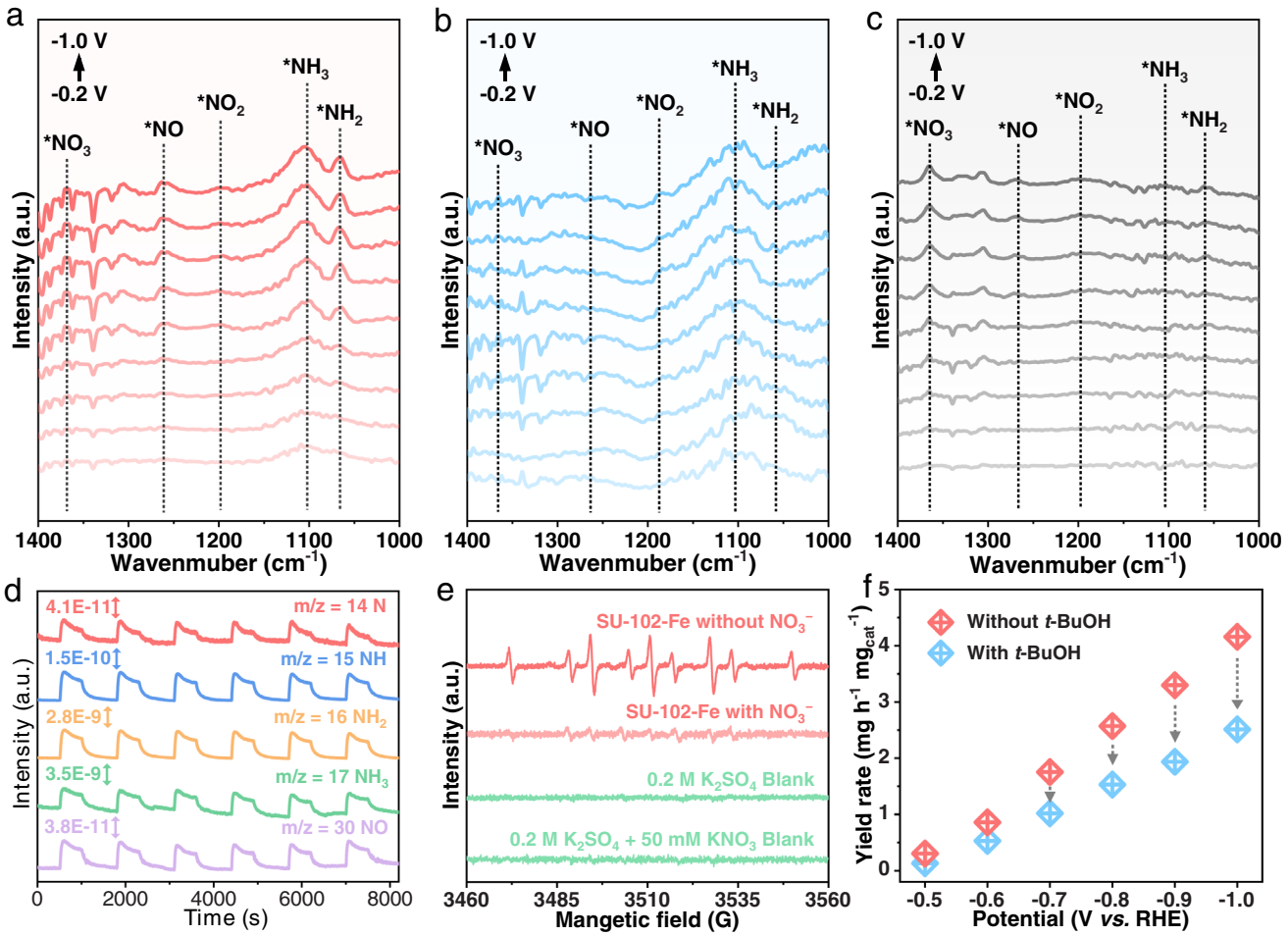

FIGURE 3 | In situ ATR-FTIR spectra of (a) SU-102-Fe, (b) Fe_2O_3 and (c) SU-102 under different applied potentials. (d) DEMS measurements of SU-102-Fe during eNO_3RR (6 cycles). (e) EPR spectra of SU-102-Fe in 0.2 M K_2SO_4 with/without NO_3^- using DMPO as the trapping agent. (f) NH_3 yield rate of SU-102-Fe at different voltages before and after adding *t*-BuOH to the electrolyte.

Notably, long-time In-situ ATR–FTIR measurements of SU-102-Fe at −0.7 V versus RHE show that all the above characteristic bands increase monotonically with electrolysis time, indicating the progressive accumulation of surface-bound intermediates and supporting their assignment (Figure S33). To exclude impurity contributions, control experiments were further conducted in nitrate-free electrolyte (MOF-only control) and in the absence of the MOF catalyst (NO_3^--only control) over a potential range from −0.2 to −1.0 V (Figures S34 and S35). In both cases, no intermediate-related bands were observed, confirming that the detected signals do not originate from impurities.

To further clarify the eNO_3RR pathway on SU-102-Fe, in situ differential electrochemical mass spectrometry (DEMS) has been conducted over six consecutive measurements (Figure S36). The prominent mass-to-charge ratio (*m/z*) signals at 2, 14, 15, 16, 17, 30, 31, 32, 33, and 46 correspond to H_2, N, NH, NH_2, NH_3, NO, NOH, NHOH, NH_2OH, and NO_2, respectively (Figures 3d and S37). Notably, ^{15}N-labeled in-situ DEMS experiments show that all nitrogen-containing signals exhibit systematic +1 m/z shift relative to those obtained with $^{14}NO_3^-$, while preserving similar relative intensity trends, unambiguously confirming the nitrate-derived origin of the detected intermediates (Figures 3d and S38). In contrast, in nitrate-free electrolyte, only the H_2 signal (m/z = 2) is observed, with nitrogen-related signals being essentially absent (Figure S39), excluding contributions from nitrogen-containing impurities. The relatively weak $*NO_2$ signal and strong *NO signal suggest that $*NO_2$ is a short-lived intermediate, rapidly converting to subsequent species, consistent with the trace amount of NO_2^- observed in ATR-FTIR. Two main pathways have been proposed for NO_3^--to-NH_3 conversion in eNO_3RR: the NOH pathway and the NHO pathway. The NOH pathway proceeds via $*NO_3 \rightarrow *NO_2 \rightarrow *NO \rightarrow *NOH \rightarrow *N \rightarrow *NH \rightarrow *NH_2 \rightarrow *NH_3$ while the NHO pathway involves $*NO_3 \rightarrow *NO_2 \rightarrow *NO \rightarrow *NHO \rightarrow *NH_2O \rightarrow *NH_2OH \rightarrow *NH_2 \rightarrow *NH_3$. The observed weak $*NH_2OH$ signal, alongside strong signals for *N and *NH in the DEMS spectra indicates that the NOH pathway is the dominant route. Together with ATR-FTIR findings, these results corroborate that the eNO_3RR on SU-102-Fe predominantly follows the NOH pathway.

The above pathway involves multiple hydrogenation steps, likely facilitated by the generation and spillover of *H species. To probe the presence of *H, electron paramagnetic resonance (EPR) spectroscopy is conducted using 5,5-dimethyl-1-pyrroline-*N*-oxide (DMPO) as the radical trapping reagent (Figures 3e and S40). A clear decrease in the DMPO-H signal after eNO_3RR suggests the participation of *H in the reaction over SU-102-

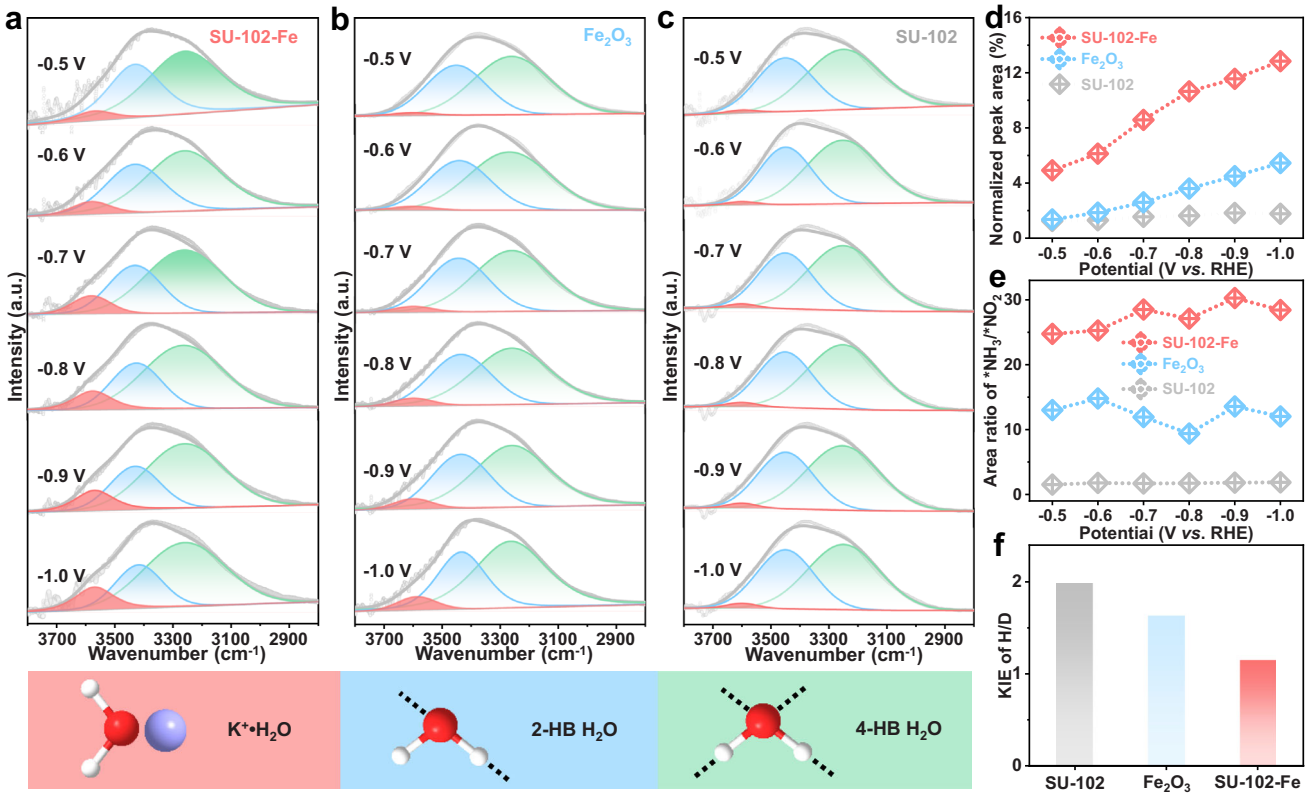

FIGURE 4 | Operando FTIR deconvoluted spectra in the 3800–2800 cm^{-1} region for (a) SU-102-Fe, (b) Fe_2O_3 and (c) SU-102 under varying applied potentials. (d) Variation trends of the operando FTIR signal assigned to $K^+ \bullet H_2O$. (e) Calculated area ratios of $*NH_3/*NO_2$ from in situ ATR–FTIR spectra (Figure 3a–c) at different applied potentials and (f) KIE measurements for SU-102-Fe, Fe_2O_3 and SU-102.

Fe. Furthermore, radical quenching experiments using tert-butyl alcohol (*t*-BuOH) as a scavenger result in a marked decline in both NH_3 yield and current density (Figures 3f and S41), further confirming the crucial role of *H in this process [64, 65].

It is assumed that the interfacial H_2O structure plays a critical role in the water dissociation step to generate *H in eNO_3RR. To investigate this, in situ ATR–FTIR is adopted. Given the complexity of interfacial H_2O, the broad —OH stretching peak (3800 to 2800 cm^{-1}) is deconvoluted into three Gaussian peaks, corresponding to tetrahedrally coordinated hydrogen-bonded H_2O (4-HB•H_2O, low-wavenumber region, green), doubly H-bonded H_2O (2-HB•H_2O, middle-wavenumber region, blue), and K^+-hydrated H_2O ($K^+ \bullet H_2O$, high-wavenumber region, red) (Figure 4a–c) [25, 66]. The normalized proportions of H_2O components on SU-102-Fe, Fe_2O_3, and SU-102 reveal that SU-102-Fe exhibits a more pronounced increase in the proportion of $K^+ \bullet H_2O$ across varying potentials (Figures 4d and S42). This observation suggests that $K^+ \bullet H_2O$ is enriched on the surface of SU-102-Fe, because its negatively charged Zr–O units attract $K^+ \bullet H_2O$ from the aqueous electrolyte solutions through electrostatic interactions [67, 68]. Therefore, maintaining a sufficient K^+ concentration is essential for the reaction. Under constant NO_3^- concentration, K^+-concentration gradient experiments show that lower K^+ levels result in reduced FE(NH_3) and NH_3 yield, along with higher FE(NO_2^-). This behavior indicates that insufficient K^+ limits the enrichment of $K^+ \bullet H_2O$ species (Figure S43). Furthermore, replacing K^+ with Na^+ or Li^+ in the electrolyte solution results in a decrease in FE(NH_3) and NH_3 yield, demonstrating that K^+ provides the most favorable environment for eNO_3RR (Figure S44).

The accumulation of $K^+ \bullet H_2O$ near Fe sites in SU-102-Fe facilitates its dissociation and generates active *H species, which is essential for NO_3^--to-NH_3 hydrogenation. At all potentials, the proportion of product ($*NH_3$) and key intermediate ($*NO_2$) in SU-102-Fe is significantly higher than that of Fe_2O_3 and SU-102, indicating that more active *H species are involved in the reaction, promoting the conversion of NO_3^- to NH_3 in the former (Figure 4e). To confirm the role of the negatively charged microenvironment around Fe sites in promoting H_2O dissociation, kinetic isotope effect (KIE) measurements are conducted using H_2O/D_2O isotope control experiments (Figure 4f). A KIE value greater than 1 generally signifies that a proton-coupled transfer step, rather than electron transfer, is rate-limiting in the electrochemical process [67, 68]. All three catalysts, SU-102-Fe, SU-102, and Fe_2O_3, display KIE values above 1, confirming that proton transfer derived from water splitting governs the reaction kinetics. Notably, SU-102-Fe exhibits a markedly smaller KIE than SU-102 and Fe_2O_3, indicating that the locally enriched $K^+ \bullet H_2O$ environment on SU-102-Fe facilitates water dissociation and thereby alleviates the kinetic barrier associated with the rate-determining step [22, 67, 69]. Moreover, the addition of bulky cations (triethylbenzylammonium, TEA^+), which partially neutralize the negatively charged MOF surface and hinder the accumulation of $K^+ \bullet H_2O$, leads to a marked decline in NH_3 FEs and yield (Figure S45a). Consistently, zeta potential measurements show that the surface potential of SU-102-Fe increases from −14.3 to −5.3 mV upon

TEA^+ addition (Figure S45b), accompanied by a pronounced decrease in Faradaic efficiency and product yield, directly corroborating the crucial role of a negatively charged microenvironment in $K^+ \bullet H_2O$ adsorption and activation. These results indicate that the catalytic performance is sensitive to the strength of the local negative charge. Further increases in cluster electronegativity may introduce additional effects or limitations but are currently constrained by the framework structure, motivating future exploration of the strength boundaries of anionic microenvironment modulation.

3 | Conclusion

In summary, an efficient electrocatalyst, SU-102-Fe, has been developed by anchoring single-atom Fe sites onto the anionic MOF SU-102 skeleton. Its crystalline porous framework ensures uniform dispersion of Fe sites, while the negatively charged Zr—O units create an anionic microenvironment that enriches weakly bonded $K^+ \bullet H_2O$ species near the single-atom Fe sites. This promotes potential-driven H_2O dissociation and improves proton supply, effectively addressing the limited H^+ availability in the NO_3^--to-NH_3 conversion. As a result, SU-102-Fe achieves excellent performance at −0.7 V versus RHE, with a FE of 96.9% and an NH_3 production rate of 1.72 mg h^{-1} mg_{cat}^{-1}, significantly outperforming the benchmark catalyst. This work underscores the potential of combining specific microenvironment with single metal atoms to develop efficient and robust electrocatalysts for sustainable nitrate reduction and ammonia synthesis.

Acknowledgments

This work was supported by the Strategic Priority Research Program of the Chinese Academy of Sciences (XDB0540000), the NSFC (22331009, 22371054, 22301045, 22405258), the Foundation of Basic and Applied Basic Research of Guangdong Province (2024A1515012801, 2024B1515120009), the Natural Science Foundation Youth Project of Anhui Province (2408085QB070), the China Postdoctoral Science Foundation (2024M753086), the Fundamental Research Funds for the Central Universities (WK9990250187) and the Key Project of Natural Science Foundation of Anhui Province (2508085ZD002). The authors thank Analysis and Test Center of Guangdong University of Technology for collecting the EPR spectra.

Conflicts of Interest

The authors declare no conflicts of interest.

Data Availability Statement

The data that support the findings of this study are available from the corresponding author upon reasonable request.

References

1. N. Lehnert, B. W. Musselman, and L. C. Seefeldt, "Grand Challenges in the Nitrogen Cycle," *Chemical Society Reviews* 50 (2021): 3640–3646, https://doi.org/10.1039/D0CS00923G.

2. X. Zhang, B. B. Ward, and D. M. Sigman, "Global Nitrogen Cycle: Critical Enzymes, Organisms, and Processes for Nitrogen Budgets and Dynamics," *Chemical Reviews* 120 (2020): 5308–5351, https://doi.org/10.1021/acs.chemrev.9b00613.

3. C. Sparacino-Watkins, J. F. Stolz, and P. Basu, "Nitrate and Periplasmic Nitrate Reductases," *Chemical Society Reviews* 43 (2014): 676–706, https://doi.org/10.1039/C3CS60249D.

4. R. B. Mellor, J. Ronnenberg, W. H. Campbell, and S. Diekmann, "Reduction of Nitrate and Nitrite in Water by Immobilized Enzymes," *Nature* 355 (1992): 717–719, https://doi.org/10.1038/355717a0.

5. M. Wu, J. Li, A. O. Leu, et al., "Anaerobic Oxidation of Propane Coupled to Nitrate Reduction by a Lineage Within the Class Symbiobacteriia," *Nature Communications* 13 (2022): 6115, https://doi.org/10.1038/s41467-022-33872-y.

6. A. P. Murphy, "Chemical Removal of Nitrate From Water," *Nature* 350 (1991): 223–225, https://doi.org/10.1038/350223a0.

7. S. Rahimi, O. Modin, and I. Mijakovic, "Technologies for Biological Removal and Recovery of Nitrogen From Wastewater," *Biotechnology Advances* 43 (2020): 107570, https://doi.org/10.1016/j.biotechadv.2020.107570.

8. C. J. Werth, C. Yan, and J. P. Troutman, "Factors Impeding Replacement of Ion Exchange With (Electro)Catalytic Treatment for Nitrate Removal From Drinking Water," *American Chemical Society Environmental Science & Technology Engineering* 1 (2021): 6–20, https://doi.org/10.1021/acsestengg.0c00076.

9. H. Xu, Y. Ma, J. Chen, W.-X. Zhang, and J. Yang, "Electrocatalytic Reduction of Nitrate—A Step towards a Sustainable Nitrogen Cycle," *Chemical Society Reviews* 51 (2022): 2710–2758, https://doi.org/10.1039/D1CS00857A.

10. Z. Zhang, Y. Lv, Y. Gu, et al., "Dual Zn_5 −NiS_4 Sites in a Redox-Active Metal–Organic Framework Enables Efficient Cascade Catalysis for Nitrate-to-Ammonia Conversion," *Angewandte Chemie International Edition* 64 (2025): e202418272, https://doi.org/10.1002/anie.202418272.

11. Q. Hu, S. Qi, Q. Huo, et al., "Designing Efficient Nitrate Reduction Electrocatalysts by Identifying and Optimizing Active Sites of Co-Based Spinels," *Journal of the American Chemical Society* 146 (2024): 2967–2976, https://doi.org/10.1021/jacs.3c06904.

12. P. Muthukumar, Z. Ullah, X. Zhang, et al., "Unlocking a Water Coordination Environment in Co-Based Metal–Organic Frameworks for Advanced Nitrate-to-Ammonia Electroreduction," *Journal of the American Chemical Society* 147 (2025): 29949–29960, https://doi.org/10.1021/jacs.5c07066.

13. G. Soloveichik, "Electrochemical Synthesis of Ammonia as a Potential Alternative to the Haber–Bosch Process," *Nature Catalysis* 2 (2019): 377–380, https://doi.org/10.1038/s41929-019-0280-0.

14. M. Wang, M. A. Khan, I. Mohsin, et al., "Can Sustainable Ammonia Synthesis Pathways Compete With Fossil-Fuel Based Haber–Bosch Processes?," *Energy & Environmental Science* 14 (2021): 2535–2548, https://doi.org/10.1039/D0EE03808C.

15. Y. Wang, C. Wang, M. Li, Y. Yu, and B. Zhang, "Nitrate Electroreduction: Mechanism Insight, In Situ Characterization, Performance Evaluation, and Challenges," *Chemical Society Reviews* 50 (2021): 6720–6733, https://doi.org/10.1039/D1CS00116G.

16. C. Zhang, Y. Zhang, R. Deng, et al., "Enabling Logistics Automation in Nanofactory: Cobalt Phosphide Embedded Metal–Organic Frameworks for Efficient Electrocatalytic Nitrate Reduction to Ammonia," *Advanced Materials* 36 (2024): 2313844, https://doi.org/10.1002/adma.202313844.

17. Y. Xiong, Y. Wang, J. Zhou, F. Liu, F. Hao, and Z. Fan, "Electrochemical Nitrate Reduction: Ammonia Synthesis and the Beyond," *Advanced Materials* 36 (2024): 2304021, https://doi.org/10.1002/adma.202304021.

18. Z. W. Seh, J. Kibsgaard, C. F. Dickens, I. Chorkendorff, J. K. Nørskov, and T. F. Jaramillo, "Combining Theory and Experiment in Electrocatalysis: Insights Into Materials Design," *Science* 355 (2017): eaad4998, https://doi.org/10.1126/science.aad4998.

19. J. Zhu, L. Hu, P. Zhao, L. Y. S. Lee, and K.-Y. Wong, "Recent Advances in Electrocatalytic Hydrogen Evolution Using Nanoparticles," *Chemical Reviews* 120 (2020): 851–918, https://doi.org/10.1021/acs.chemrev.9b00248.

20. S. Liang, X. Teng, H. Xu, L. Chen, and J. Shi, "H* Species Regulation by Mn-Co$(OH)_2$ for Efficient Nitrate Electro-Reduction in Neutral Solution," *Angewandte Chemie International Edition* 63 (2024): e202400206, https://doi.org/10.1002/anie.202400206.

21. W. Liao, J. Wang, G. Ni, et al., "Sustainable Conversion of Alkaline Nitrate to Ammonia at Activities Greater Than 2 A cm^{-2}," *Nature Communications* 15 (2024): 1264, https://doi.org/10.1038/s41467-024-45534-2.

22. Y. Wan, M. Pei, Y. Tang, et al., "Interfacial Water Regulation for Nitrate Electroreduction to Ammonia at Ultralow Overpotentials," *Advanced Materials* 37 (2025): 2417696, https://doi.org/10.1002/adma.202417696.

23. D. T. Bregante, M. C. Chan, J. Z. Tan, et al., "The Shape of Water in Zeolites and Its Impact on Epoxidation Catalysis," *Nature Catalysis* 4 (2021): 797–808, https://doi.org/10.1038/s41929-021-00672-4.

24. P. Li, Y. Jiang, Y. Hu, et al., "Hydrogen Bond Network Connectivity in the Electric Double Layer Dominates the Kinetic pH Effect in Hydrogen Electrocatalysis on Pt," *Nature Catalysis* 5 (2022): 900–911, https://doi.org/10.1038/s41929-022-00846-8.

25. L. F. Scatena, M. G. Brown, and G. L. Richmond, "Water at Hydrophobic Surfaces: Weak Hydrogen Bonding and Strong Orientation Effects," *Science* 292 (2001): 908–912, https://doi.org/10.1126/science.1059514.

26. Y. Wang, F. Hao, H. Xu, et al., "Interfacial Water Structure Modulation on Unconventional Phase Non-Precious Metal Alloy Nanostructures for Efficient Nitrate Electroreduction to Ammonia in Neutral Media," *Angewandte Chemie International Edition* 64 (2025): e202508617, https://doi.org/10.1002/anie.202508617.

27. S.-J. Zheng, X.-Y. Dong, H. Chen, R.-W. Huang, J. Cai, and S.-Q. Zang, "Unveiling Ionized Interfacial Water-Induced Localized H* Enrichment for Electrocatalytic Nitrate Reduction," *Angewandte Chemie International Edition* 64 (2025): e202413033, https://doi.org/10.1002/anie.202413033.

28. X.-Y. Wang, Y.-Z. Pan, J. Yang, et al., "Single-Atom Iron Catalyst as an Advanced Redox Mediator for Anodic Oxidation of Organic Electrosynthesis," *Angewandte Chemie International Edition* 63 (2024): e202404295, https://doi.org/10.1002/anie.202404295.

29. J. Xu, S. Zhang, H. Liu, et al., "Breaking Local Charge Symmetry of Iron Single Atoms for Efficient Electrocatalytic Nitrate Reduction to Ammonia," *Angewandte Chemie International Edition* 62 (2023): e202308044, https://doi.org/10.1002/anie.202308044.

30. B. Chang, Z. Cao, Y. Ren, et al., "Electronic Perturbation of Isolated Fe Coordination Structure for Enhanced Nitrogen Fixation," *American Chemical Society Nano* 18 (2024): 288–298, https://doi.org/10.1021/acsnano.3c06212.

31. Y. Zang, D.-Q. Lu, K. Wang, et al., "A Pyrolysis-Free Ni/Fe Bimetallic Electrocatalyst for Overall Water Splitting," *Nature Communications* 14 (2023): 1792, https://doi.org/10.1038/s41467-023-37530-9.

32. O. M. Yaghi, G. Li, and H. Li, "Selective Binding and Removal of Guests in a Microporous Metal–Organic Framework," *Nature* 378 (1995): 703–706, https://doi.org/10.1038/378703a0.

33. S. Horike and S. Kitagawa, "The Development of Molecule-Based Porous Material Families and Their Future Prospects," *Nature Materials* 21 (2022): 983–985, https://doi.org/10.1038/s41563-022-01346-7. PMID: 36002726.

34. J. Liu, T. A. Goetjen, Q. Wang, et al., "MOF-Enabled Confinement and Related Effects for Chemical Catalyst Presentation and Utilization," *Chemical Society Reviews* 51 (2022): 1045–1097, https://doi.org/10.1039/D1CS00968K.

35. C. Chen, L. Shen, B. Wang, et al., "Environmental Applications of Metal–Organic Framework-Based Three-Dimensional Macrostructures: A Review," *Chemical Society Reviews* 54 (2025): 2208–2245, https://doi.org/10.1039/D4CS00435C.

36. X. Zhao, Y. Wang, D.-S. Li, X. Bu, and P. Feng, "Metal–Organic Frameworks for Separation," *Advanced Materials* 30 (2018): 1705189, https://doi.org/10.1002/adma.201705189.

37. H. Wang, Y. Liu, and J. Li, "Designer Metal–Organic Frameworks for Size-Exclusion-Based Hydrocarbon Separations: Progress and Challenges," *Advanced Materials* 32 (2020): 2002603, https://doi.org/10.1002/adma.202002603.

38. L. Jiao and H.-L. Jiang, "Metal-Organic Frameworks for Catalysis: Fundamentals and Future Prospects," *Chinese Journal of Catalysis* 45 (2023): 1–5, https://doi.org/10.1016/S1872-2067(22)64193-7.

39. V. V. Gusev, D. Adamson, A. Deligkas, et al., "Optimality Guarantees for Crystal Structure Prediction," *Nature* 619 (2023): 68–72, https://doi.org/10.1038/s41586-023-06071-y.

40. Q.-J. Wu, J. Liang, Y.-B. Huang, and R. Cao, "Thermo-, Electro-, and Photocatalytic CO_2 Conversion to Value-Added Products Over Porous Metal/Covalent Organic Frameworks," *Accounts of Chemical Research* 55 (2022): 2978–2997, https://doi.org/10.1021/acs.accounts.2c00326.

41. W. Zhao, Y. Shi, Y. Jiang, et al., "Fe-O Clusters Anchored on Nodes of Metal–Organic Frameworks for Direct Methane Oxidation," *Angewandte Chemie International Edition* 60 (2021): 5811, https://doi.org/10.1002/anie.202013807.

42. J.-Y. Li, J.-R. Huang, Z.-H. Zhao, H.-L. Zhu, P.-Q. Liao, and X.-M. Chen, "Low-Coordination Indium Single-Atom Sites Anchored on a Metal-Organic Framework Single-Layer Boosts Electroreduction of CO_2 Into Formic Acid," *Angewandte Chemie International Edition* 137 (2025): e202511132.

43. L. Jiao and H.-L. Jiang, "Metal-Organic-Framework-Based Single-Atom Catalysts for Energy Applications," *Chemistry* 5 (2019): 786–804, https://doi.org/10.1016/j.chempr.2018.12.011.

44. H. He, L. Hashemi, M.-L. Hu, and A. Morsali, "The Role of the Counter-Ion in Metal-Organic Frameworks' Chemistry and Applications," *Coordination Chemistry Reviews* 376 (2018): 319–347, https://doi.org/10.1016/j.ccr.2018.08.014.

45. S. S. Park, Y. Tulchinsky, and M. Dincă, "Single-Ion Li^+, Na^+, and Mg^{2+} Solid Electrolytes Supported by a Mesoporous Anionic Cu–Azolate Metal–Organic Framework," *Journal of the American Chemical Society* 139 (2017): 13260–13263, https://doi.org/10.1021/jacs.7b06197.

46. S.-N. Zhao, Y. Zhang, S.-Y. Song, and H.-J. Zhang, "Design Strategies and Applications of Charged Metal Organic Frameworks," *Coordination Chemistry Reviews* 398 (2019): 113007, https://doi.org/10.1016/j.ccr.2019.07.004.

47. L. Jiao, J. Wang, and H.-L. Jiang, "Microenvironment Modulation in Metal–Organic Framework-Based Catalysis," *Accounts of Materials Research* 2 (2021): 327–339, https://doi.org/10.1021/accountsmr.1c00009.

48. E. S. Grape, A. J. Chacón-García, S. Rojas, et al., "Removal of Pharmaceutical Pollutants From Effluent by a Plant-Based Metal–Organic Framework," *Nature Water* 1 (2023): 433–442, https://doi.org/10.1038/s44221-023-00070-z.

49. Z. Chen, A. Huang, K. Yu, et al., "Fe_1 N_4 $-O_1$ Site With Axial Fe–O Coordination for Highly Selective CO_2 Reduction Over a Wide Potential Range," *Energy & Environmental Science* 14 (2021): 3430–3437, https://doi.org/10.1039/D1EE00569C.

50. V. G. Chandrashekhar, T. Senthamarai, R. G. Kadam, et al., "Silica-supported Fe/Fe–O Nanoparticles for the Catalytic Hydrogenation of Nitriles to Amines in the Presence of Aluminium Additives," *Nature Catalysis* 5 (2022): 20–29, https://doi.org/10.1038/s41929-021-00722-x.

51. P. H. Langevelde, I. Katsounaros, and M. T. M. Koper, "Electrocatalytic Nitrate Reduction for Sustainable Ammonia Production," *Joule* 5 (2021): 290–294, https://doi.org/10.1016/j.joule.2020.12.025.

52. W. Duan, Y. Li, Y. Ou, et al., "Insights Into Electrochemical Nitrate Reduction to Nitrogen on Metal Catalysts for Wastewater Treatment," *Environmental Science & Technology* 59 (2025): 3263–3275, https://doi.org/10.1021/acs.est.4c09975.

53. Y.-J. Shih, Z.-L. Wu, and Y.-C. He, "Tuning Transition Metals Layered-Electroplated on Bimetallic MxCu1−X Crystallites (M = Fe, Co, Ni, and Zn) to Boost Ammonia Yield in Electrocatalytic Reduction of Nitrate

Wastewaters," *Journal of Hazardous Materials* 477 (2024): 135276, https://doi.org/10.1016/j.jhazmat.2024.135276.

54. C. Lu, Y. Chen, C. Shuang, et al., "Simultaneous Removal of Nitrate Nitrogen and Orthophosphate by Electroreduction and Electrochemical Precipitation," *Water Research* 250 (2024): 121000, https://doi.org/10.1016/j.watres.2023.121000.

55. S. Z. Andersen, V. Čolić, S. Yang, et al., "A Rigorous Electrochemical Ammonia Synthesis Protocol With Quantitative Isotope Measurements," *Nature* 570 (2019): 504–508, https://doi.org/10.1038/s41586-019-1260-x.

56. Y. Yang, L. Zhang, Z. Hu, et al., "The Crucial Role of Charge Accumulation and Spin Polarization in Activating Carbon-Based Catalysts for Electrocatalytic Nitrogen Reduction," *Angewandte Chemie International Edition* 59 (2020): 4525–4531, https://doi.org/10.1002/anie.201915001.

57. M. C. Figueiredo, J. Souza-Garcia, V. Climent, and J. M. Feliu, "Nitrate Reduction on Pt(111) Surfaces Modified by Bi Adatoms," *Electrochemistry Communications* 11 (2009): 1760–1763, https://doi.org/10.1016/j.elecom.2009.07.010.

58. S. Zhang, K. Li, X. Zhang, et al., "Concurrently Selective Electrosynthesis of Ammonia and Glycolic Acid over Cathodic Single-Atom Cobalt and Anodic PdNi Alloying Catalysts," *Advanced Functional Materials* 35 (2025): 2415046, https://doi.org/10.1002/adfm.202415046.

59. Y. Li, Q. Zhang, H. Dai, D. He, Z. Ke, and X. Xiao, "Photoelectrochemical Nitrate Denitrification Towards Acidic Ammonia Synthesis on Copper-Decorated Black Silicon," *Energy & Environmental Science* 17 (2024): 9233–9243, https://doi.org/10.1039/D4EE04438J.

60. Y. Wei, J. Huang, H. Chen, et al., "Electrocatalytic Nitrate Reduction on Metallic CoNi-Terminated Catalyst With Industrial-Level Current Density in Neutral Medium," *Advanced Materials* 36 (2024): 2404774, https://doi.org/10.1002/adma.202404774.

61. H. Xiao, M. Xia, B. Chong, H. Li, B. Lin, and G. Yang, "D-Band Center Modulation of B-mediated FeS_2 to Activate Molecular Nitrogen for Electrocatalytic Ammonia Synthesis," *Applied Catalysis B: Environmental* 343 (2024): 123474, https://doi.org/10.1016/j.apcatb.2023.123474.

62. R. Zhang, C. Li, H. Cui, et al., "Electrochemical Nitrate Reduction in Acid Enables High-Efficiency Ammonia Synthesis and High-Voltage Pollutes-Based Fuel Cells," *Nature Communications* 14 (2023): 8036, https://doi.org/10.1038/s41467-023-43897-6.

63. Y. Zhang, T. Gao, F. Zhang, et al., "Regioselective Doping Into Atomically Aligned Core–Shell Structures for Electrocatalytic Reduction of Nitrate to Ammonia," *Advanced Energy Materials* 14 (2024): 2401834, https://doi.org/10.1002/aenm.202401834.

64. G. V. Buxton, C. L. Greenstock, W. P. Helman, and A. B. Ross, "Critical Review of Rate Constants for Reactions of Hydrated Electrons, Hydrogen Atoms and Hydroxyl Radicals (·OH/·O− in Aqueous Solution," *Journal of Physical and Chemical Reference Data* 17 (1988): 513–886, https://doi.org/10.1063/1.555805.

65. K. Yang, S.-H. Han, C. Cheng, C. Guo, T. Li, and Y. Yu, "Unveiling the Reaction Mechanism of Nitrate Reduction to Ammonia over Cobalt-Based Electrocatalysts," *Journal of the American Chemical Society* 146 (2024): 12976–12983, https://doi.org/10.1021/jacs.3c13517.

66. J. Ni, J. Yan, F. Li, et al., "Atomic Co—P Catalytic Pair Drives Efficient Electrochemical Nitrate Reduction to Ammonia," *Advanced Energy Materials* 14 (2024): 2400065, https://doi.org/10.1002/aenm.202400065.

67. Q. Hu, K. Yang, O. Peng, et al., "Ammonia Electrosynthesis From Nitrate Using a Ruthenium–Copper Cocatalyst System: A Full Concentration Range Study," *Journal of the American Chemical Society* 146 (2024): 668–676, https://doi.org/10.1021/jacs.3c10516.

68. S. Hammes-Schiffer, "Explaining Kinetic Isotope Effects in Proton-Coupled Electron Transfer Reactions," *Accounts of Chemical Research* 58 (2025): 1335–1344, https://doi.org/10.1021/acs.accounts.5c00119.

69. Q. Hu, C. Shang, X. Chen, et al., "Subnanometric Nickel Phosphide Heteroclusters With Highly Active $Ni^{\delta+}$ –$P^{\delta-}$ Pairs for Nitrate Reduction Toward Ammonia," *Journal of the American Chemical Society* 147 (2025): 12228–12238, https://doi.org/10.1021/jacs.5c01455.

Supporting Information

Additional supporting information can be found online in the Supporting Information section.

Supporting File: anie72024-sup-0001-SuppMat.docx.